Numerical simulations and experimental measurements of dense-core vortex rings in a sharply stratified environment

2013 Comput. Sci. Disc. 6 014001

(http://iopscience.iop.org/1749-4699/6/1/014001)

COMPUTATIONAL SCIENCE&DISCOVERY

Numerical simulations and experimental measurements of dense-core vortex rings in a sharply stratified environment

R Camassa, S Khatri, R McLaughlin, K Mertens, D Nenon, C Smith and C Viotti

Carolina Center for Interdisciplinary Applied Mathematics, Department of Mathematics and UNC Joint Fluids Lab, University of North Carolina at Chapel Hill, Chapel Hill, NC, USA
E-mail: rmm@email.unc.edu

Received 24 April 2012, in final form 24 October 2012
Published 4 January 2013
Computational Science & Discovery **6** (2013) 014001 (17pp)
doi:10.1088/1749-4699/6/1/014001

Abstract. We present three-dimensional direct numerical simulations of a vortex ring settling in sharply stratified miscible ambient fluids for near two-layer configurations, and comparisons of these simulations with the results from laboratory experiments. The core fluid of the vortex rings has density higher than both the top and the bottom layers of the ambient fluid, and is fully miscible in both layers. This setup ensures a rich parameter space that we partially explore in this study. In particular, a critical (bifurcation) phenomenon is identified that distinguishes the long-time behavior of the settling vortex ring as either being fully trapped at the ambient density layer or continuing through the layer in its downward motion. This critical behavior is determined by the initial conditions (e.g. the size and speed of the vortex ring, the initial distance to the layer, etc). The numerical simulations are able to provide evidence for this in qualitative agreement with an experimental phase diagram. Our setup isolates essential elements of mixing, trapping and escape through stratified fluids in a variety of situations, such as the mixing and dispersion of pollutants and plankton in the ocean.

Contents

1. Introduction

Vertical density stratifications are prevalent in both the atmosphere and the ocean. These background stratifications strongly influence the mixing and dispersion properties of the fluid and particles passing through them [1, 2]. In some instances these can cause the trapping of particulate matter for long periods of time at locations where they alone are not neutrally buoyant. The recent oil spill in the Gulf provides one such example, demonstrating subsurface plumes, initially much less dense than sea water, trapping for months several hundreds of meters below the surface. Another example is the thin layer formation of marine snow aggregates, particles composed of organic and inorganic matter, which has a significant role in the marine carbon cycle [3, 4].

All of these applications involve the dynamics of fluids dragged by either solid particles or self-advected in the form of vortices through different density ambient fluids. Much insight can be gained by studying the simplified setup of a single particle or vortex ring dynamics. In recent years, experimental and theoretical progress has been made on this problem for the case of a single sphere falling through sharp stratification at both moderate Reynolds numbers (300) [5, 6] and low Reynolds numbers (0.001) [7, 8]. In particular, at moderate Reynolds, Abaid *et al* [6] demonstrated experimentally that a dense falling sphere could, in fact, reverse direction and rise on a transient time scale as a plume of light fluid carried by the sphere detached. Further, at low Reynolds numbers, Camassa *et al* [7, 8] in a series of papers demonstrated both experimentally and theoretically that the falling sphere could undershoot the terminal velocity of the bottom layer, with theory providing fully quantified predictions of the sphere and fluid dynamics for the entire evolution.

Considerably less is known about miscible dense vortex rings falling through stratified fluids. In homogeneous ambient fluids, when a dense fluid droplet falls under the influence of gravity into a bath of a lighter miscible fluid, a vortex ring is formed and can remain stable to a fairly large penetration depth [9, 10].

Starting from the seminal work by Thomson and Newall [11], many studies have looked at single- and two-fluid experiments in this setting. For example, experimental reports concerning the low Reynolds number limit can be found in [12], and examples at moderate Reynolds number can be found in [9, 10, 13]. For the single-fluid system, much work has also been done in modeling vortex ring dynamics and instabilities (the works [14–19] give a thorough but in no way complete list of commonly cited papers). The focus of the present study is on the behavior arising from the addition of an ambient sharp stratification. A special case of this setup was studied by Dahm *et al* [20], in which an ambient two-layer fluid was considered, while the vortex

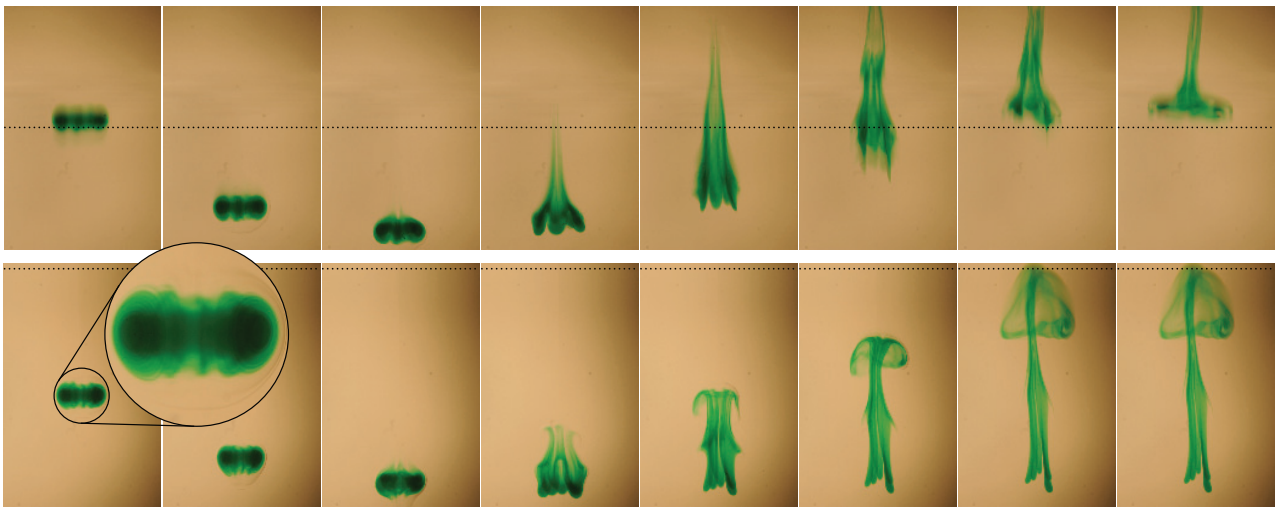

Figure 1. Time lapse of a vortex ring for the two behaviors described in section 5. The dotted horizontal line in each montage shows the approximate depth of the bottom of the background density transition.

ring density matched that of the top layer. Further studies of this special case are examined experimentally in [21, 22] and numerically in [23].

Here, we explore the richer regime involving three distinct densities in which the vortex ring is denser than all ambient fluid. In this case, if a dense vortex ring encounters a sharp density ambient fluid transition before reaching its destabilization length scale, the interaction can be nontrivial and potentially lead to the total entrapment of the vortex fluid within this density transition layer. We remark that in earlier two-layer studies [20] involving a vortex density matched to top layer density, this is the only possible outcome, while here it remains possible that some vortex rings may continue propagating downward beyond the ambient fluid density transition. This process is exemplified experimentally in figure 1, where a sequence of snapshots of a saltwater vortex ring is settling in a salt stratified environment. Two different outcomes are demonstrated: (i) the vortex ring penetrates below the density transition layer and then rebounds upward settling at the interface between the two layers, and (ii) the vortex ring continues to settle into the lower layer after penetration and eventually releases the entrained fluid well within the lower layer. This critical phenomenon is the focus of this study.

With the advancement of computational power in recent decades, more sophisticated methods have been developed to delve into the rich and complicated behavior of the vortex ring problem through direct simulations. In the 1980s, with computational power still somewhat limited, most work was done in two dimensions, and with strongly simplified ansatz, boundary integral methods were most commonly used [24, 25]. In the 1990s, more advanced simulations began to appear, including vortex sheet methods [26–29] and viscous-dominated axisymmetric Navier–Stokes solvers [30]. More recently, access to more realistic three-dimensional computations have started to become available [23]. These simulations have allowed for deeper probing into these complicated dynamics, restricted to the case involving a two-layer ambient fluid with the vortex ring density matched to that of the top layer. The present study adds the new element of a vortex ring density, which is different from (denser than) all ambient fluids. We compare fully three-dimensional variable density Navier–Stokes simulations to experiments for the case of fully miscible three density systems at moderate Reynolds numbers (of the order of 10^2).

This setup poses a challenging task for direct numerical simulations. The numerical solver must be capable of solving the three-dimensional, varying density, incompressible Navier–Stokes equations, and of efficiently resolving the fine structures (filamentation) that result from the dynamics of the interacting varying-density fluids. In this respect, note that even in a homogeneous ambient fluid, the fluid entrainment that follows vortex ring dynamics poses significant difficulties because of fine-scale structures that must be resolved [23, 28, 31]. Ultimately, diffusion of the stratifying agent will set a cutoff for small-scale filamentation, and its proper inclusion may play a role in the long-time complete mixing observed in some of the experiments.

Fortunately, given the time and length scales of this particular experiment (typically in the order of seconds), direct numerical simulations do appear capable of resolving the fine structure in the evolution of vortex rings in stratified fluids (albeit taking on the order of days for a single parallel simulation on a cluster). A further complexity arising here concerns the initialization of the vortex ring when comparing to experimental data, and will be discussed below.

In our case, an appropriate and convenient choice of a solver suitable for the numerical issues sketched above is offered by the VARDEN numerical code [32]. For the initialization of the numerical simulations, we use Hill's spherical vortex solution while tuning its free parameters to match the experimentally observed radius and velocity at a given position.

In this paper, we begin by introducing the problem and the governing equations. The numerical methods used to conduct direct numerical simulations of the full three-dimensional variable density Navier–Stokes equations are described in detail. These simulations will then be used to reproduce the critical phenomena of trap and escape which are observed in the experiments. We first focus on the preliminary case of a dense vortex ring in a homogeneous ambient fluid and then probe the rich physical scenario ensuing from the interaction of the vortex ring and the ambient density transition layer.

2. Governing equations

The governing equations for a stratified, incompressible fluid with variable density are the following Navier–Stokes equations:

$$\begin{aligned} &(\rho\mathbf{u})_t + (\mathbf{u}\cdot\nabla)(\rho\mathbf{u}) = -\nabla p - g\rho\hat{\mathbf{z}} + \mu\nabla^2\mathbf{u}, \\ &\rho_t + \mathbf{u}\cdot\nabla\rho = 0, \\ &\nabla\cdot\mathbf{u} = 0, \end{aligned} \tag{1}$$

where $\mathbf{u}$, ρ and p are the fluid velocity, density and pressure, respectively. The parameters in the equations above include the dynamic viscosity of the fluid, μ, and the gravitational acceleration, g. The underlying assumptions are that the dynamics take place on a scale fast enough to neglect diffusivity of the stratifying agents and have sufficiently small Mach numbers to justify the assumption of incompressibility. Our fluids, being stratified with salt, do not involve any surface tension effects.

We consider a three-dimensional computational domain with periodic lateral boundary conditions on a square in the horizontal direction for both the velocity and density fields. On the top and bottom walls of the fluid domain, the velocity field has no slip boundary conditions and the density field has no flux boundary conditions. Such boundary conditions only approximately represent the true physical boundary conditions, which in a fixed container should be no slip for velocity and no flux for density on all fixed walls. With a sufficiently large computational domain the assumptions of periodicity are often a good approximation to the experimental setup.

The initial conditions are chosen to emulate those of the experiment which involve an initial vortex ring, with a given radius and velocity, whose core density is higher than all ambient fluid densities (described below in more detail). We remark that the initialization of the vortex velocity and density field to reflect that of the experiment is a subtle issue, mainly due to experimental uncertainties.

The ambient fluid is either homogeneous or a stably stratified two-layer fluid. A schematic diagram of the two situations in which we present experimental and numerical results is shown in figure 2. The first case (left panel), in which a dense vortex ring settles in an ambient homogenous fluid, is used as a quantified, benchmark comparison between the experiments and the numerical simulations. Subsequently, more complicated phenomena emerging from a sharp background stratification (right panel) will be presented and compared with the data from a refined experimental campaign. The latter numerical studies, while preliminary, predict a striking critical phenomenon observed in the experiments.

While in the experiment the density transition between the top and bottom ambient fluid layers has finite thickness, the numerical simulations are carried out with a step density transition. We have conducted a preliminary numerical study which shows that modifying the transition layer to have a small finite thickness

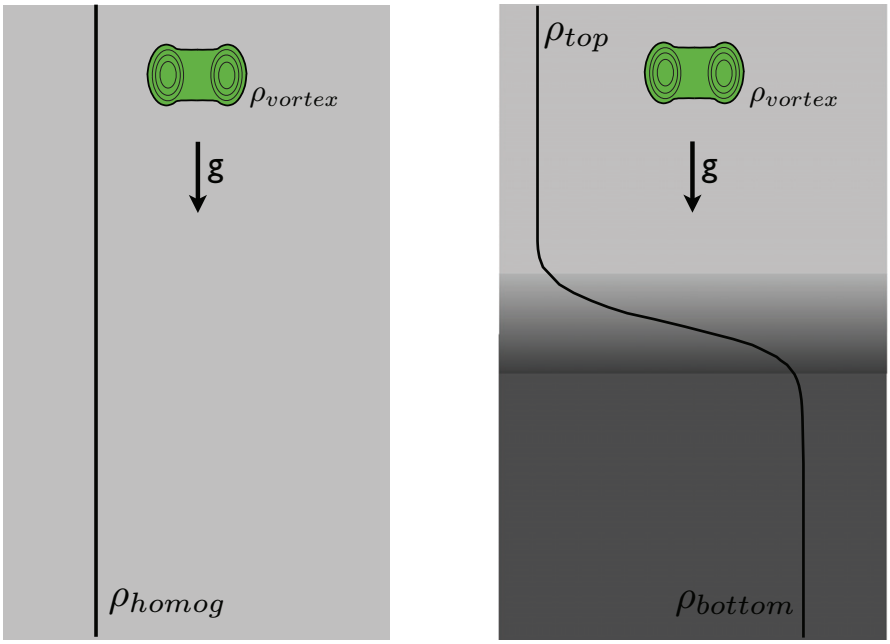

Figure 2. Schematic diagram of the two cases presented in this paper. A vortex ring with density, ρ_{vortex}, settling in a homogeneous ambient fluid with density, $\rho_{\text{homog}} < \rho_{\text{vortex}}$, is shown on the left. On the right, a vortex ring with density, ρ_{vortex}, settling into a sharply stratified ambient fluid is shown. The top layer has density, ρ_{top}, and the bottom layer has density, ρ_{bottom}, with $\rho_{\text{top}} < \rho_{\text{bottom}} < \rho_{\text{vortex}}$. Here, we show a transition layer of finite thickness between the two densities, as occurs in experiments, but the numerical modeling is performed with zero thickness.

does not predict significantly different results from those presented here. Arbitrary length scale transitions will be considered in future work.

For this problem, we nondimensionalize the Navier–Stokes equations, equation (1), using the initial vortex ring radius, R_{v}, as the length scale, $\sqrt{R_{\text{v}}/g}$ as the time scale and either the homogenous ambient density, ρ_{homog}, or the top layer ambient density, ρ_{top}, as the density scale, which gives

$$\begin{aligned} &(\rho\mathbf{u})_t + (\mathbf{u}\cdot\nabla)(\rho\mathbf{u}) = -\nabla p - \tfrac{1}{Fr^2}\rho\hat{\mathbf{z}} + \tfrac{1}{Re}\nabla^2\mathbf{u}, \\ &\rho_t + \mathbf{u}\cdot\nabla\rho = 0, \\ &\nabla\cdot\mathbf{u} = 0, \end{aligned} \tag{2}$$

where $\mathbf{u}$, ρ and p are now the nondimensional fluid velocity, density and pressure, respectively. The nondimensional numbers in the equations above are the Reynolds number, Re, the ratio of inertial forces to viscous forces, and the Froude number, Fr, the ratio of inertial forces to gravitational forces. Throughout this paper, the density scale, whether in a homogeneous or two-layer ambient case, is taken to be equal to the density of freshwater, $0.997\,\text{g}\,\text{cc}^{-1}$.

3. Numerical methods

For numerical simulations we employ a modified version of the software VARDEN developed at Lawrence Berkeley National Lab [32]. We chose to use VARDEN as it is a reliable state-of-the-art numerical code implemented for three-dimensional large-scale parallel computations that can handle variable density incompressible flows. The numerical scheme implemented in VARDEN is an approximate projection method, which employs a multigrid iterative linear solver to enforce incompressibility up to a prescribed tolerance. The advection terms in the momentum and density equations are discretized using a conservative second-order upwind scheme, with robustness properties suitable for nondiffusive density advection and even applicable in the limit of inviscid flows. Temporal evolution uses an adaptive time step set by user-defined tolerances.

For stability, momentum diffusion is treated implicitly with a Crank–Nicholson scheme. Further details of the method can be found in [32]. The simulations we perform have approximately 10^8 grid points and take about one day to run (in wall-clock time) on a local UNC cluster typically running on 256, 2.93 GHz Intel processors. In the rectangular geometry described above, we employ uniform rectangular meshes. Each time step generates output files of approximately 2.5 Gb, and postprocessing the ensuing large dataset is efficiently handled using the Data Tank software package [33].

3.1. Initial conditions

To initialize the numerical simulations, the ambient fluid consists of either a constant density fluid for the full computational domain or a sharply stratified two-layer fluid with a step function transition at a prescribed height. To initiate a downward propagating vortex ring, the velocity field is initialized using Hill's spherical vortex exact solution [34]. This is a steady solution for homogeneous and inviscid fluids obtained by matching a rotational flow inside a sphere of nondimensional radius one with an outer potential flow, to enforce continuity of velocity and pressure. Inside the sphere, the initial nondimensional density, ρ_v, is set to a constant value higher than all ambient densities, and consequently, these initial data are not an exact solution of either the inviscid or viscous dynamics. In this work, we adopt the laboratory reference system, in which the vortex travels with a vertical initial nondimensional velocity, U_0. In the ensuing evolution the vortex ring expands and entrains ambient fluid, according to the general features of vortex ring dynamics. This will be illustrated and discussed below.

In three dimensions, Hill's solution is expressed in terms of a suitably defined axial-symmetric streamfunction. The solution is

$$\psi(h,z) = \begin{cases} \dfrac{3}{4}U_0h^2\left(1-r^2\right)+\dfrac{1}{2}h^2U_0 & \text{for } r<1, \\ -\dfrac{1}{2}U_0h^2\left(1-\dfrac{1}{r^3}\right)+\dfrac{1}{2}h^2U_0 & \text{for } r>1, \end{cases} \tag{3}$$

where h is the distance from the axis of symmetry and $r=\sqrt{h^2+(z-z_d)^2}$ is the distance from the center of the sphere, (x_d, y_d, z_d). The radial and vertical velocity components, respectively, u_h and w, are given by

$$-\frac{1}{h}\frac{\partial\psi}{\partial z}=u_h, \quad \frac{1}{h}\frac{\partial\psi}{\partial h}=w.$$

Therefore, in Cartesian coordinates, the corresponding velocity field is

$$\mathbf{u}=\frac{3}{2}U_0\left((x-x_d)(z-z_d), \quad (y-y_d)(z-z_d), \quad 1-(r^2+h^2)+\frac{2}{3}\right)$$

for $r<1$, and

$$\mathbf{u}=\frac{3}{2}U_0\left(\frac{(x-x_d)(z-z_d)}{r^5}, \quad \frac{(y-y_d)(z-z_d)}{r^5}, \quad \frac{2}{3}\frac{1}{r^3}-\frac{h^2}{r^5}\right)$$

for $r>1$. In figure 3, the streamlines of the three-dimensional Hill's spherical vortex ring solution in the x–z plane can be seen.

In order to compare numerical simulations with laboratory experiments, we need to reproduce initial conditions for the radius, velocity and density of the vortex ring that match the properties of the experimental vortex rings after their formation process is completed. The procedure that we follow to obtain such initialization parameters is described in section 5.2.

4. Simulations

We next present numerical simulations using the setup described above over a range of physical parameters matching experiments. First, we focus on the case of a homogeneous ambient fluid. We conduct a numerical

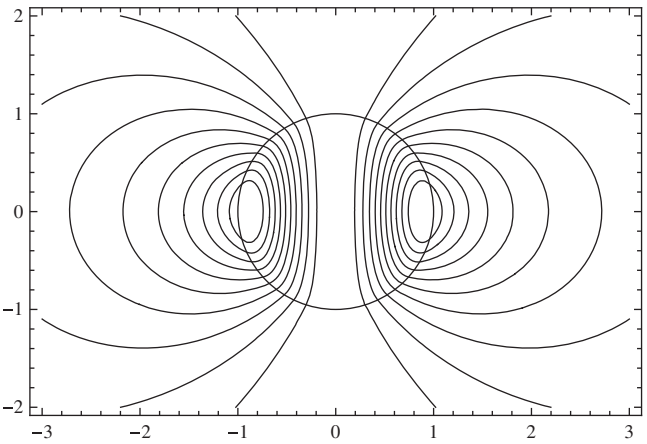

Figure 3. Instantaneous streamlines in the laboratory frame of the Hill's three-dimensional spherical vortex on the x–z coordinate plane.

convergence study and a domain size study using this case. Also, with this situation, quantified comparisons with the experiments are provided. Then, the results are shown for the more complex dynamics arising from a sharp ambient stable stratification.

In the numerical results presented here, we plot depth versus time, velocity versus time and radius versus time. To define the depth of the vortex ring in the vertical direction (z dimension), we first average the density in the x–y direction and then locate the maximum of this averaged density in the z-direction. In practice, this means that the position of the vortex ring is defined to be where the core is located, where the density is the greatest. We then evaluate the velocity by taking the discrete time derivative of the depth. Finally, to define a radius for the vortex ring, a slice of the density field through the center of the domain is considered and the extrema of the derivative of the density along the position line of the vortex ring on this slice give the diameter.

4.1. Convergence study of the numerical method

VARDEN has been used to model numerous different fluid phenomena and in many cases convergence studies of the code have been presented [35, 36], as well as in the original development of the code [32]. Here, we present a convergence study for one of the homogeneous ambient cases shown below. In this simulation, we are studying a vortex ring with density, $\rho_v = 1.0231$, settling in an ambient homogeneous fluid. The initial downward velocity is $U_0 = 0.7004$. In this convergence study the volume of the domain is $L_H \times L_H \times 4L_H$ with horizontal length $L_H = 11$. Rectangular grids are used with meshsize $h \times h \times h$ where $h = 2^{-N} L_H$ and $N = 6, 7, 8$.

In figure 4, we show the nondimensional depth and velocity of the core and the radial growth of the vortex ring as a function of time. We show the results until time $t = 140$, which is prior to the time scale on which Rayleigh–Taylor instabilities begin to cause the vortex ring to become unstable with the parameters set as in this study, discussed further below in section 5.1. These plots demonstrate convergence as N increases and allow us to make a good choice for the resolution in the more complex situation involving two-layer ambient stratification.

Through the resolution study, we are able to observe a decrease of numerical diffusion as the resolution increases. This is also observed when using finer grids in cases with an ambient two-layer sharp stratification. This decrease of numerical diffusion allows for finer scale density structures to form and persist in the case of finer grids. Since molecular diffusion of the stratifying agent has been neglected, the numerical diffusion is providing the mixing that occurs between fluids with varying density once the fine structures are below the length scale of the numerical diffusion, which does depend on the resolution. In the simulations, this mixing is considered to be numerical error depending on the grid size since we are solving the equations without molecular diffusion. This is an acceptable approximation as the dynamics of this problem are occurring on time scales that are fast enough in comparison with the diffusion time scales of the stratifying agent.

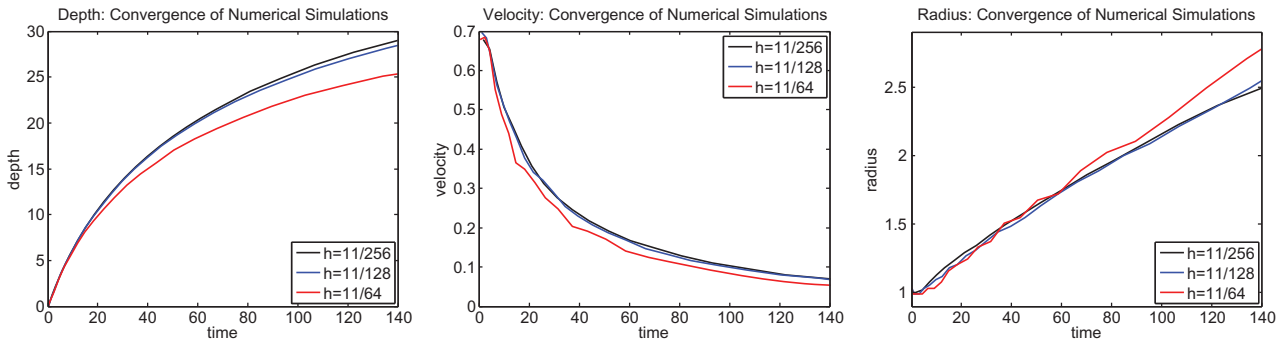

Figure 4. Results of a convergence study of a vortex ring with density 1.0231 settling in a homogeneous ambient fluid. Three varying resolutions are shown here.

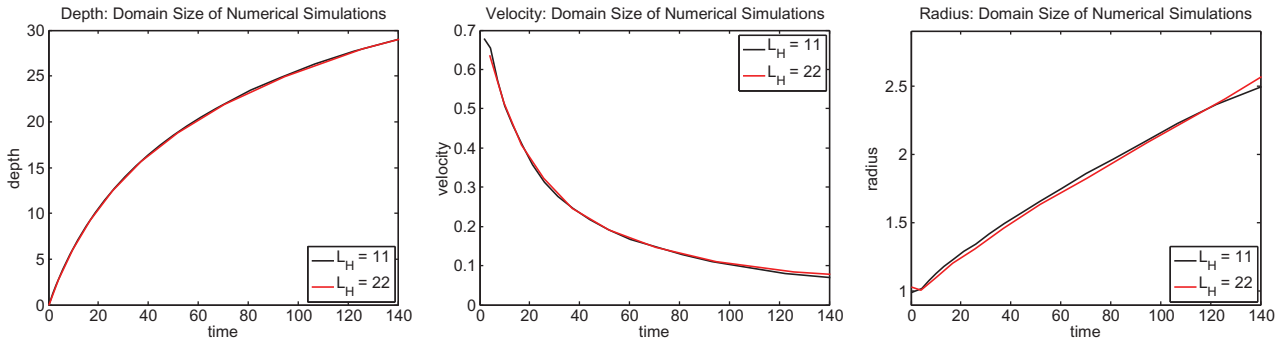

Figure 5. The results of a domain size study of a vortex ring with density 1.0231 settling in a homogeneous ambient fluid. Two different domain sizes with the same resolution are shown here.

Of course, the final stages of mixing, once the filamentation length scale reaches the molecular diffusion scale, would require explicitly modeling the molecular diffusion.

4.2. Domain size study

We now present a domain size study for the same case as in the convergence study. The results are shown in figure 5 for two different domain sizes, $L_{\mathrm{H}} = 11$ and 22 (run with the same grid resolution, $h = 11/128$). From these simulations, we can confirm that the periodic boundary conditions in the horizontal direction are not affecting the results significantly.

5. Vortex ring experiments and comparisons with simulations

In this section, the vortex ring experiments will be described in detail, and compared quantitatively with numerical simulations in the homogeneous cases, and qualitatively in the more complex cases involving sharp stratification. While we will identify several obstacles to obtaining agreement (primarily due to vortex initialization), we nonetheless see reasonable comparisons in each case presented below.

5.1. Experimental setup

Experiments are carried out in a tank filled with either homogeneous or two constant density layers separated by a sharp density transition.

The experiment initialization of miscible vortex rings with fluid densities higher than the ambient fluid presents a nontrivial challenge. The standard piston injection procedure fails due to fluid leakage and mixing before piston actuation. A diaphragm (gate) would alleviate this, but besides being an added technological complication, this further introduces spurious fluid motion in contact with the moving surfaces. A simpler

Table 1. Droplet weight and radius measurements. The data are based on 35 realizations.

Density (g cc^{-1})	Mass (g)	Std dev.	Average radius (cm)	Std dev.
0.998 34	0.087 02	0.000 69	0.160 79	0.000 2
1.021 23	0.083 74	0.000 56	0.157 65	0.000 32
1.039 79	0.079 28	0.000 64	0.153 84	0.000 38

alternative is to use drops of varying density released from a prescribed height (typically 26 mm) above the free surface. In this way, after the drop splashes through the free surface, a coherent dense vortex ring forms in a repeatable manner after undergoing a shedding process near the free surface (see figure 1).

This particular height was selected as it maximizes the penetration depth by minimizing the eccentricity on impact, due to shape oscillations arising from surface tension forces for a droplet falling in air after its release [9]. Through empirical studies, we observed that the ideal configuration for the most coherent vortex ring occurs when the droplet impacts the surface transitioning from spherical to prolate spheroidal shape. This procedure leads to impact velocities of the order of 10–15 cm s^{-1}, so that the initial Reynolds number is approximately 300–450. The droplets were created using a medical IV line connected to a small pipet. The IV line was then connected to a syringe attached to a precision manual linear drive, which allowed for very regular droplet creation. A table of droplet sizes can be found in table 1.

The fluids used for these experiments were all deionized water and mixtures of salt water. We add food coloring to the fluid drops that are released above the free surface to allow us to visualize the resulting vortex rings. An Anton Parr DMA 4500 density meter with accuracy up to 5×10^{-5} g cc^{-1} was used to measure fluid densities, while a WTW Cond 197i and Orion 550A conductivity probe (with a cell constant of $0.475 \pm 1.5\%$) was used to measure density profiles within the stratified tanks.

For the visualization of the vortex ring evolution, a Photron Fastcam with a resolution of 512×480 pixels (leading to roughly 100 px cm^{-1} resolution) and a frame rate of 125 fps was used. This setup gave enough spatial resolution to accurately determine the depth and velocity of the vortex ring. Also, measurements of radial growth as the vortex ring propagates downward are made using the same setup. Depth and radial measurements in the experiment are made using intensity and gradients of intensity in the images, since the vortex ring fluid is dyed while the ambient is not. The velocity of the vortex ring propagation is evaluated by taking a discrete time derivative of the depth data, smoothing using a ten-point moving average. Additionally, high-resolution still-shot images were taken to explore more carefully the internal detail using a Nikon D3 and macro lens that gives a resolution of up to 1000 px cm^{-1} at 8 fps.

In general, the experiment outlined contains eight dimensional parameters: the vortex ring density, the top layer density, the bottom layer density, the droplet radius, the drop release height above the free surface, the top layer thickness, the bottom layer thickness and the density transition thickness. In the case of a homogeneous ambient fluid, the bottom and top densities are equal and there is no ambient density transition. In this work however, we only consider a two-dimensional subspace by holding all the parameters fixed except the density of the vortex ring and the top layer thickness.

There exists a maximum depth of penetration for a dense miscible vortex ring descending through a homogeneous fluid before the ring becomes unstable and breaks apart [9, 10]. The first set of experiments quantifies this maximum penetration length scale in a homogeneous ambient fluid. This maximum penetration exists because vortex rings in viscous fluids spread and slow down so that Rayleigh–Taylor instabilities can arise leading to the demise of the dense core. This length scale is important because it sets the upper bound for top layer thicknesses, which can be investigated in the ambient sharply stratified case. Hence, in this set of experiments the nondimensional density of the vortex ring, ρ_v, is varied. These simpler experiments are also used for comparison with the direct numerical simulations, verifying that the code can accurately predict the velocity and position of the vortex ring, as well as qualitatively predict the growth of the radii. Figure 10 shows this destabilization length scale experimentally as a function of increasing vortex ring density.

Having established the destabilization length scale, we next introduce a sharp stratification and investigate how this modifies the overall dynamics of the stable descending vortex ring. For this second set of experiments, the nondimensional top layer thickness, H_t, is varied from 5 to 60, the nondimensional bottom layer density

is $\rho_b = 1.023$ and the ρ_v varies from 1.023 to 1.043. In these experiments, the nondimensional density transition layer thickness is approximately 8. For a three-density system (with 1 as the top layer density after nondimensionalization) ordered as $1 < \rho_b < \rho_v$, two broad classes of dynamic behavior are found, signifying a critical phenomenon of entrapment or escape, as demonstrated in figure 1.

5.2. The initial condition problem for the simulations

Quantitative comparison of a numerical simulation with a specific experiment, as mentioned above, requires an appropriate initial condition for the dimensional velocity, radius, R_v and density of the Hill's spherical vortex ring. The radius, R_v, provides the length scale of the problem, while the nondimensional velocity, U_0, and density, ρ_v, are initialized directly in the simulations. This information is not directly available from the present experimental setup owing to the complex vortex formation processes associated with impacting the free surface. Image analysis provides partial information on these parameters, but is imprecise on account of ambient fluid entrainment, optical aberrations and dye dispersion. We choose initial numerical values for the radius and velocity based on the imaged experimental vortex ring radius and velocity shortly after the drop has passed through the free surface and rolled into a vortex ring. During this process, the drop sheds a minimal amount of fluid which can be visually perceived. Unless otherwise noted, the dimensional radius and velocity are measured in the experiment once the vortex ring has travelled approximately 3–3.5 mm after this shedding process has occurred. For the density, we choose to set the Hill's spherical vortex ring density, ρ_v, based on the initial experimental drop density. Very often, experiments with identical conditions were replicated numerous times. In these cases, the average values of the measured radii and velocities were used to set the initial conditions of the simulation with identical parameters.

The position of the vortex ring and the resulting behaviors as it evolves in time are highly dependent on the initialization of the vortex ring. In the numerical simulations, we are using the inviscid steady-state solution, the Hill's spherical vortex ring, to initialize the problem. By using this initial condition, we are assuming that the vortex ring is quickly evolving into a solution of the viscous variable density Navier–Stokes equations. Thus, we set the radius and velocity in the initial Hill's vortex ring in the simulations based on the fully formed vortex ring observed in the experiments.

Ideally, it would be desirable to set the initial conditions of the numerical simulations on a fully developed viscous solution emanating from the Hill spherical vortex or another exact solution. Lacking full experimental information regarding the evolving velocity and density field and a numerical procedure for carrying out a precise initial condition matching, we defer this improvement to future studies.

5.3. Vortex ring dynamics: a homogeneous environment

To verify the numerical simulations conducted using the methodology presented in section 3, we first compare the simulations and experiments of vortex rings descending in a homogeneous ambient fluid. To compare a simulation with a set of experiments, the ambient fluid density is set as in the experiments and the initial vortex radius, velocity and density are set as described in section 5.2.

In figure 6, the position and velocity of the descending vortex ring averaged over ten identical experiments (red lines) and the position and velocity of the vortex ring in numerical simulations (black lines) are shown. The black solid lines in the plots are the depth and velocity measured based on density, as described in section 4. The black dashed lines are depth measured based on vorticity, since in the case of a fully homogeneous setup density differences cannot be used to measure physical quantities. When using vorticity, the depth of the vortex ring is set to be the z-coordinate of the location of the maximum and minimum vorticity components coming out of the plane on a slice down the center of the domain.

These simulations are initialized with three different density vortex rings, $\rho_v = 1$, 1.0231 and 1.0431, being released in a homogeneous ambient fluid. Following the initialization procedure discussed in section 5.2, we set the initial radius of the Hill's vortex ring to $R_v = 0.22$, 0.225 and 0.204 cm, which sets the length scales of the simulations, respectively. The initial downward velocity is set to $U_0 = 0.627$, 0.700 and 0.707, respectively. In these simulations, the domain size is set to $L_H \times L_H \times 4L_H$, where $L_H = 11$, and the grid resolution is set to $h = 11/256$.

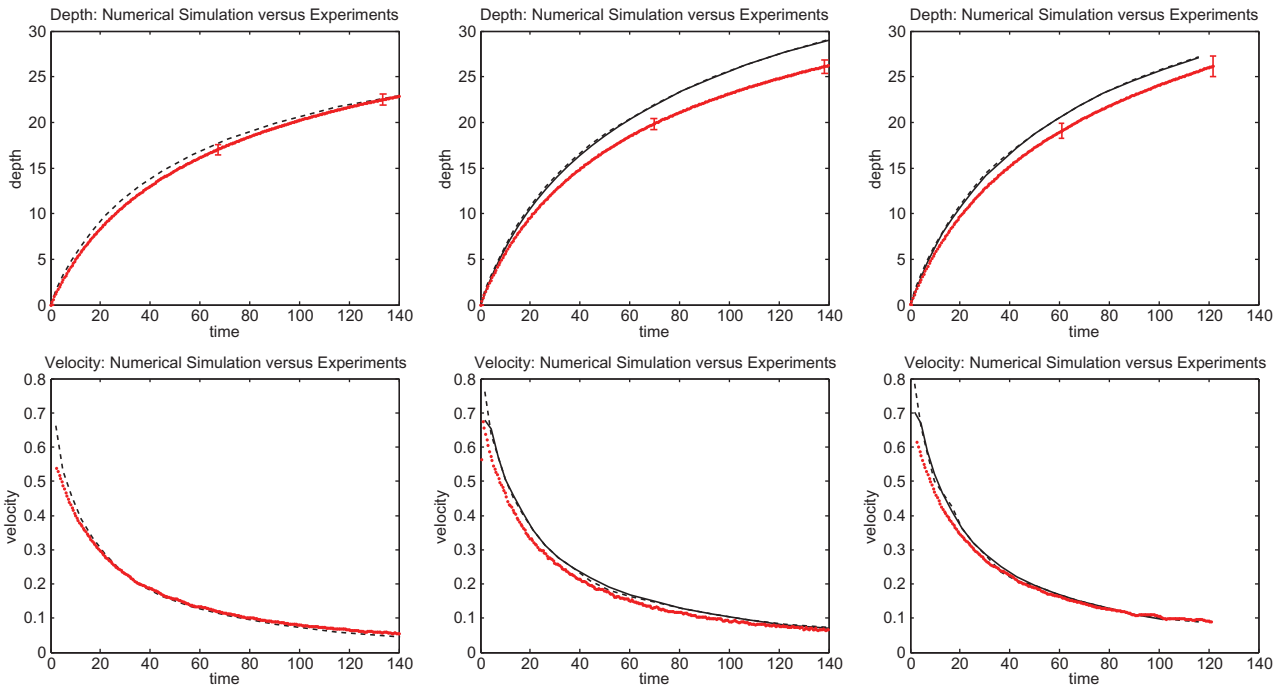

Figure 6. Comparisons of simulations (black lines) and experiments (red lines) of varying density vortex rings settling in a homogeneous ambient fluid. The left column shows results where the vortex ring has been initialized with density 1, the middle column with a vortex ring initialized with density 1.0231 and the right column with a vortex ring initialized with density 1.0431. Solid lines represent measurements made based on density and dashed lines represent measurements based on vorticity. Error bars for depth represent an approximate 95% confidence interval.

As can be seen from figure 6, there is reasonable quantitative agreement between the simulation and the experiments, which confirms the methodology of the simulations presented here. The numerical simulations accurately capture the behavior of the vortex ring as it descends. Note that the initial velocity is slightly different in the simulation with respect to the experimental values. This discrepancy is most likely due to the difficulty of setting the initial conditions, as described in section 5.2.

In figure 7, the radius versus time is presented for both experiments and numerical simulations. Note that here the radius of the vortex ring in the numerical simulations is measured using both density (as described above) and vorticity. When using vorticity, we take the radius to be the distance between the location of the out of plane maximum and minimum vorticity in the vortex symmetry plane. Observe the qualitative agreement between experiments and simulations: the radius growth rate in both cases increases as the initial vortex core density increases. Note that the different vortex radius metrics used give slightly different measurements (radii measured using vorticity are less than the measured radii using density, since the locations of the maximum and minimum vorticity component used to measure these radii are in the interior of the vortex ring). In the experiments, the image resolution and dye dispersion make measuring the radius as a function of time a challenging task. Some of the discrepancy between the numerics and the experiments may be due to this lack of accuracy in measuring the experimental radii.

In the right panel of the figure, we show a wide range of different initial vortex ring densities. Surprisingly, a slight change in this density from the fully homogeneous case results in a large change in the growth rate of the ring. For the fully homogenous experiment, $\rho_v = 1.000$, the actual physical density is slightly larger than the ambient fluid (a nondimensional increase of approximately 0.0002) due to the vortex ring fluid being dyed. This slight increase in density may be one reason why the radius growth rate in the experimental homogeneous case is larger than what is observed in the numerical simulations.

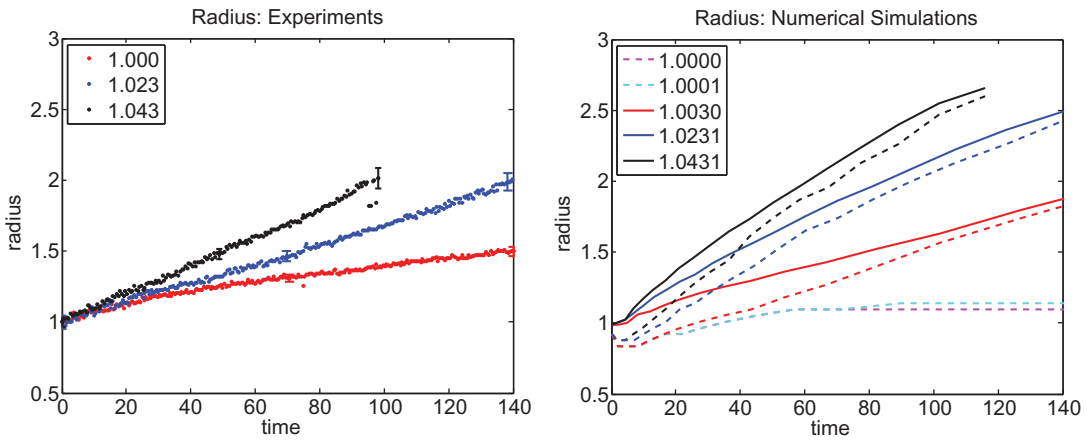

Figure 7. Evolution of experimental (left) and computational (right) vortex ring radii. The legends indicate the initial vortex ring densities. In the right panel, dashed lines indicate radii measured based on vorticity and solid lines indicate radii measured tracking the density. Error bars for the experiments represent an approximate 95% confidence interval.

5.4. Vortex ring dynamics: a sharply stratified density gradient

In this section, we present numerical computations including a sharp internal stratification in the domain. We now set an upper layer density of 1, as for the unstratified case, above a lower layer where $\rho_b = 1.02$. We consider a vortex ring of initial density, $\rho_v = 1.03$. This choice is motivated by the experiments. The experiments demonstrate that there is a critical behavior, summarized in the phase diagram shown in figure 10. The critical top layer thickness is dependent on the difference between the initial density of the vortex ring and the bottom layer density.

In the following computations, the size of the computational domain is set to be $L_H \times L_H \times 5L_H$ with $L_H = 8$, with a mesh size $h = 8/256$. Two cases will be presented here, demonstrating an escaping vortex ring and a trapping vortex ring. For both cases, the length scale is set to $R_v = 0.12\,\text{cm}$ and the initial nondimensional velocity of the Hill's vortex is $U_0 = 2.3053$. For the escape case, the density transition is located 14 nondimensional length units below the center of the initial vortex ring. For the second case, the density transition is located 26 nondimensional length units below the center of the Hill's spherical vortex at $t = 0$.

In figure 8, a time series of the first case is presented. Level sets of intermediate density values (gray equaling near bottom layer density values of 1.018, and green equaling near core density values of 1.025) are shown. This case documents the complete escape of a vortex ring through the density transition. In contrast, figure 9 presents the second case demonstrating transient trapping. As the vortex ring passes through the density transition, the entrainment bubble of the light upper fluid carries all of the dense core back into the density transition region. On longer time scales, a lack of finer grid resolution and the absence of molecular diffusion leads to a small region of nonmixed higher density fluid, which then falls through into the lower layer. This last detail does not match the observed experimental outcome, which shows complete mixing and no final rain out phase. However, the numerical outcome is not unexpected in view of not explicitly including molecular diffusion in the computation as well as the step function stratification employed in the present study. The effect of the transition layer thickness in the ambient stratification has been explored for the case of a rigid falling sphere in our ongoing experiments with similar density differences. In these studies, increasing thicknesses diminish the effectiveness of the entrained fluid in arresting the body. In the vortex ring case, it is reasonable to expect that this would correspond to an increased mixing of the vortex ring plus entrained top layer fluid with the bottom, denser fluid. While we have seen that a slightly thicker density transition does not modify our findings greatly, more refined studies with arbitrary thicknesses are in progress and this will be the subject of a future report. In the phase diagram, figure 10, the locations of these two numerical simulations have been marked for reference.

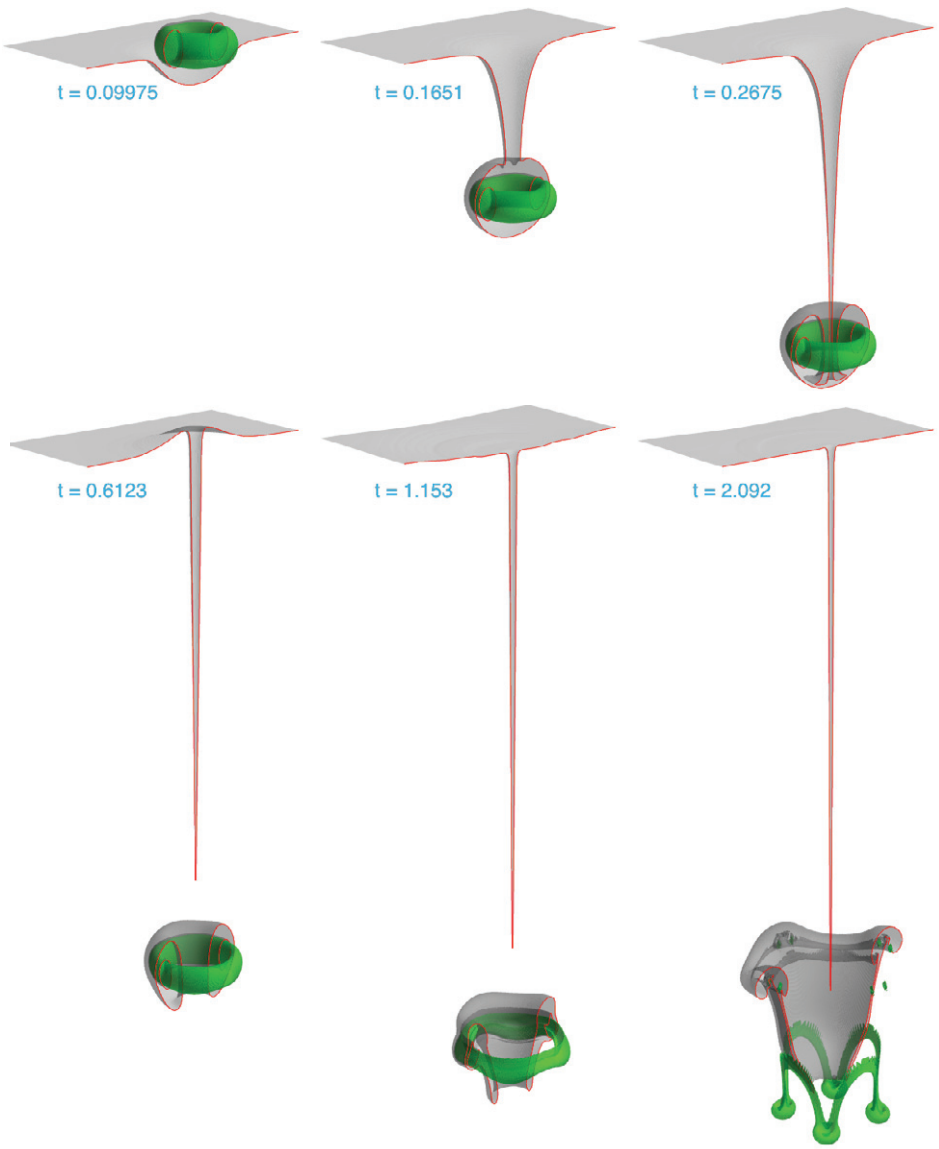

Figure 8. Vortex escaping through the internal stratification, visualized by density isosurfaces. In these snapshots, green is where $\rho = 1.025$ and gray is where $\rho = 1.018$. Note that the fine scale structure evident in the last time step is an artifact of the rendering levelset software.

5.5. Critical phenomena: entrapment versus escape

A rough theoretical prediction for the critical length scale between escape and trapping phenomena, which emphasizes the importance of entrainment, can be seen through a simple scaling argument. The density of the conglomerate mixture, ρ_{mix}, of the droplet fluid and the ambient fluid may be estimated as a ratio of the total mass to the total volume, $\rho_{\text{mix}} = (\rho_{\text{v}} V_0 + (V - V_0))/V$, where ρ_{v}, V_0 and V are the respective nondimensional initial density, initial volume of the vortex ring and total (growing) vortex ring volume. As this mixture impinges upon a sharp density transition, a critical length scale may be deduced by equating the vortex-ring mixture density with the limiting density across the transition layer, ρ_{b}, $V_{\text{e}}/V_0 = (\rho_{\text{v}} - \rho_{\text{b}})/(\rho_{\text{b}} - 1)$, where the entrainment volume is $V_{\text{e}} = V - V_0$. Experimental measurements of the propagation speed of vortex rings [37] have shown that the velocity decreases in time as $\frac{\text{d}Z}{\text{d}t} \sim t^{-1/3}$. Integrating yields the depth growing as $Z \sim t^{2/3}$. Vortex rings in homogeneous environments are known to grow linearly in time with the propagation distance due to viscosity [38]. With this observation of linearly growing rings, $V_{\text{e}} \sim t$, we may calculate the

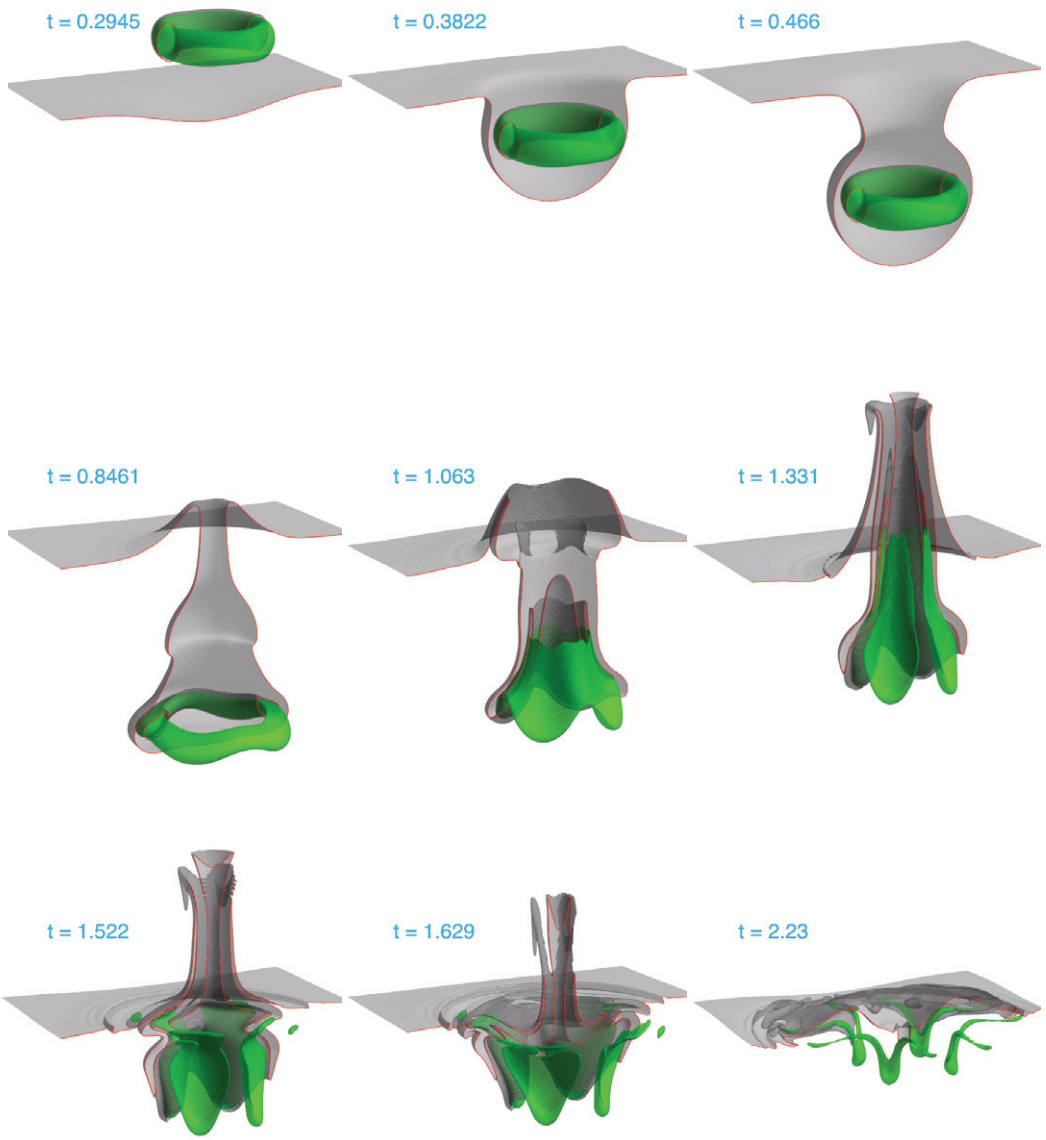

Figure 9. Vortex trapping through the internal stratification, visualized by density isosurfaces. In these snapshots, green is where $\rho = 1.025$ and gray is where $\rho = 1.018$.

critical length scale $Z \sim (\rho_v - \rho_b)^{2/3}$. Figure 10 shows the critical height as a function of the density difference obtained by experiments and the results are compared with this power-law prediction.

6. Conclusions

In closing, this paper presents direct numerical simulations and comparisons with data from experiments concerning the dynamics of a dense vortex ring descending through a sharply stratified density transition. It is found that a range of critical parameters exist for which a vortex ring, initially more dense than either of the two underlying layers, can still become totally trapped within the sharp transition region.

It is seen that the entrained bubble of the top layer fluid carried by the vortex ring into the transition layer plays a significant role in the criticality trapping/escaping phenomenon by creating a buoyancy-driven rebound. This creates filamentation in the rebounding fluid, which enhances diffusion and hence

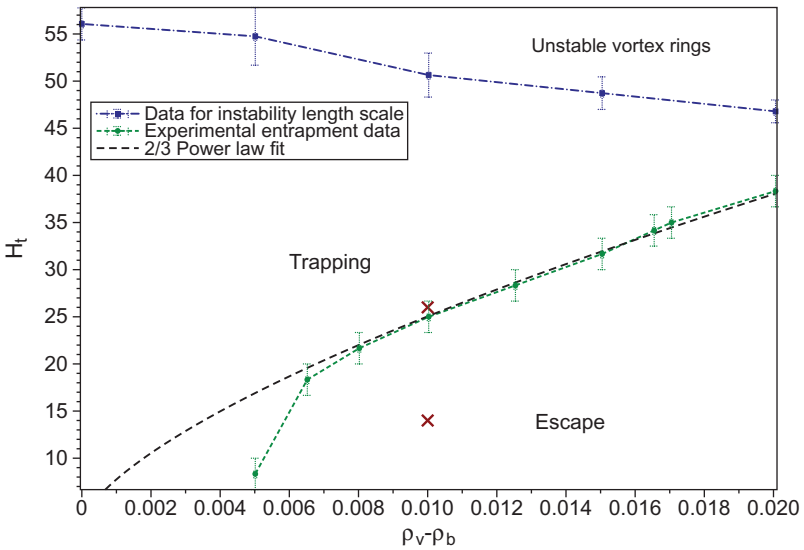

Figure 10. Vortex ring critical length for trapping found from experiments; also shown in blue is the length of travel at which a vortex ring becomes unstable in a homogenous fluid, as well as the two-thirds scaling law prediction fit, which ignores the outlier which has a critical length that falls within the density transition thickness. Also shown (red crosses) are the locations in the phase diagram of the companion numerical simulations. Note that the nondimensional top layer thickness, H_t, in the experimental data shown is measured from the free surface, whereas a fully formed vortex ring does not emerge until several radii below the free surface.

wipes out buoyancy differences. Our direct numerical simulations of the three-dimensional variable density Navier–Stokes equations are compared with experimental results and confirm the critical escape/trapping phenomena summarized in an experimental phase diagram. These results demonstrate the capability of large-scale computing to produce quantified predictions of some complex stratified fluid behavior.

This investigation sheds light on the applicability of direct numerical simulations to physical problems of great importance, such as mixing in stratified jets and plumes, central to numerous environmental and geophysical problems (see [39] for an example of plume formation in oil spills), and may provide an improved understanding of more complex oceanic mixing processes. In fact, blobs of sedimenting particulate often behave in a fashion resembling vortex rings and exhibit similar dynamics. The computational and experimental studies presented here demonstrate a novel critical phenomenon which has immediate real-world applications, particularly concerning the ocean carbon pump. Recent observations have demonstrated an accumulation of marine snow particulate matter in regions of strong vertical density variation [3]. This suggests that the fundamental fluid dynamics behind the trapping phenomena studied here may be central to a complete understanding of the ocean carbon budget. Future work will be directed at further understanding similar phenomena in more complex environments.

Acknowledgments

We thank David Adalsteinsson and DataTank, Ann Almgren and VARDEN, and David Holz for his assistance with the experiments and for his suggestions for improving visualization techniques. We further acknowledge undergraduate laboratory assistance from C Mosley and M Hemphill. We thank Brian White for helpful discussions. DN and CS gratefully acknowledge undergraduate research assistantship through NSF RTG DMS-0943851 and NSF RTG DMS-0502266. This research was supported by NSF RTG DMS-0502266, NSF RTG DMS-0943851, NSF RAPID CBET-1045653, NSF CMG ARC-1025523 and NSF DMS-1009750 and the Office of Naval Research for support through ONR DURIP N00014-09-1-0840.

References

[1] Simons G A and Larson R S 1974 Formation of vortex rings in a stratified atmosphere *Phys. Fluids* **17** 8–14
[2] Tailleux R 2009 On the energetics of stratified turbulent mixing, irreversible thermodynamics, Boussinesq models and the ocean heat engine controversy *J. Fluid Mech.* **638** 339–82
[3] MacIntyre S, Alldredge A L and Gotschalk C C 1995 Accumulation of marine snow at density discontinuities in the water column *Limnol. Oceanogr.* **40** 449–68
[4] Alldredge A L, Cowles T J, MacIntyre S, Rines J E B, Donaghay P L, Greenlaw C F, Holliday D V, Dekshenieks M M, Sullivan J M and Zanevald J R V 2002 Occurrence and mechanisms of formation of a dramatic thin layer of marine snow in a shallow Pacific fjord *Mar. Ecol. Prog. Ser.* **233** 1–12
[5] Srdic-Mitrovic A N, Mohamed N A and Fernando H J S 1999 Gravitational settling of particles through density interfaces *J. Fluid Mech.* **381** 175–98
[6] Abaid N, Adalsteinsson D, Agyapong A and McLaughlin R M 2004 An internal splash: levitation of falling spheres in stratified fluids *Phys. Fluids* **16** 1567–80
[7] Camassa R, Falcon C, Lin J, McLaughlin R M and Parker R 2009 Prolonged residence times for particles settling through stratified miscible fluids in the Stokes regime *Phys. Fluids* **21** 031702
[8] Camassa R, Falcon C, Lin J, McLaughlin R M and Mykins N 2010 A first-principle predictive theory for a sphere falling through sharply stratified fluid at low Reynolds numbers *J. Fluid Mech.* **664** 436–65
[9] Chapman D S and Critchlow P R 1967 Formation of vortex rings from falling drops *J. Fluid Mech.* **29** 177–85
[10] Baumann N, Joseph D D, Mohr P and Renardy Y 1992 Vortex rings of one fluid in another in free fall *Phys. Fluids* A **4** 567–80
[11] Thomson J J and Newall H F 1885 On the formation of vortex rings by drops falling into liquids and some allied phenomena *Proc. R. Soc. Lond.* **39** 417–36
[12] Koh C J and Leal L G 1990 An experimental investigation on the stability of viscous drops translating through a quiescent fluid *Phys. Fluids* A **2** 2103–9
[13] Maxworthy T 1974 Turbulent vortex rings *J. Fluid Mech.* **64** 227–39
[14] Akhmetov D G 2008 Model of vortex ring formation *J. Appl. Math. Tech. Phys.* **49** 909–18
[15] Norbury J 1973 A family of steady vortex rings *J. Fluid Mech.* **57** 417–31
[16] Kojima M, Hinch E J and Acrivos A 1984 The formation and expansion of a toroidal drop moving in a viscous fluid *Phys. Fluids* **27** 19–32
[17] Fraenkel L 1972 Examples of steady vortex rings of small cross-section in an ideal fluid *J. Fluid Mech.* **51** 119–35
[18] Pullin D I and Saffman P G 1998 Vortex dynamics in turbulence *Annu. Rev. Fluid Mech.* **30** 31–51
[19] Maxworthy T 1977 Some experimental studies of vortex rings *J. Fluid Mech.* **81** 465–95
[20] Dahm W J A, Scheil C M and Tryggvason G 1989 Dynamics of vortex interaction with a density interfaces *J. Fluid Mech.* **205** 1–43
[21] Linden P F 1973 The interaction of a vortex ring with a sharp density interface: a model for turbulent entrainment *J. Fluid Mech.* **60** 467–80
[22] Dandy D S and Leal L G 1989 Buoyancy-driven motion of a deformable drop through a quiescent liquid at intermediate Reynolds numbers *J. Fluid Mech.* **208** 161–92
[23] Stock M, Dahm W and Tryggvason G 2008 Impact of a vortex ring on a density interface using a regularized inviscid vortex sheet method *J. Comput. Phys.* **227** 9021–43
[24] Pozrikidis C 1990 The instability of a moving viscous drop *J. Fluid Mech.* **210** 1–21
[25] Zinemanas D and Nir A 1988 On the viscous deformation of biological cells under anisotropic surface tension *J. Fluid Mech.* **193** 217–41
[26] Nitsche M and Krasny R 1994 A numerical study of vortex ring formation at the edge of a circular tube *J. Fluid Mech.* **276** 139–61
[27] Lindsay K and Krasny R 2001 A particle method and adaptive treecode for vortex sheet motion in three-dimensional flows *J. Comput. Phys.* **172** 879–907
[28] Feng H, Kaganovskiy L and Krasny R 2009 Azimuthal instability of a vortex ring computed by a vortex sheet panel method *Fluid Dyn. Res.* **41** 051405
[29] Tryggvason G, Unverdi S O, Song M and Abdollahi-Alibeik J 1991 Interaction of vortices with a free surface and density interfaces *Vortex Dynamics and Vortex Methods* ed C Anderson and C Greengard (*Lectures in Applied Mathematics* vol 28) (Providence, RI: American Mathematical Society) pp 679–99
[30] Marcus D L and Bell J B 1994 Numerical simulation of a viscous vortex ring interaction with a density interface *Phys. Fluids* **6** 1505–14

[31] Dritschel D G 1989 Contour dynamics and contour surgery: numerical algorithms for extended, high-resolution modeling of vortex dynamics in two-dimensional, inviscid, incompressible flows *Comput. Phys. Rep.* **10** 77–146
[32] Almgren A, Bell J, Colella P, Howell L and Welcome M 1998 A conservative adaptive projection method for the variable density incompressible Navier–Stokes equations *J. Comput. Phys.* **142** 1–46
[33] Adalsteinsson D 2012 *Datatank* http://visualdatatools.com
[34] Lamb H 1997 *Hydrodynamics* (Cambridge: Cambridge University Press)
[35] Camassa R and Viotti C 2012 On the response to upstream disturbances of large amplitude internal waves *J. Fluid Mech.* **702** 59–88
[36] Almgren A, Camassa R and Tiron R 2012 Shear instabilities of internal solitary waves in Euler fluids with thin pycnoclines *J. Fluid Mech.* **710** 324–61
[37] Dabiri J O and Gharib M 2004 Fluid entrainment by isolated vortex rings *J. Fluid Mech.* **511** 311–31
[38] Maxworthy T 1972 The structure and stability of vortex rings *J. Fluid Mech.* **51** 15–32
[39] Adalsteinsson D, Camassa R, Harenberg S, Lin Z, McLaughlin R M, Mertens K, Reis J, Schlieper W and White B 2011 Subsurface trapping of oil plumes in stratification: laboratory investigations *Monitoring and Modeling the Deepwater Horizon Oil Spill: A Record-Breaking Enterprise* (*Geophysical Monograph Series* vol 195) (Washington, DC: American Geophysical Union) pp 257–62